Whole Tissue Imaging of Cellular Boundaries at Sub-Micron Resolutions for Automatic Cell Segmentation: Applications in Epithelial Bending of Ectodermal Appendages

Sam Norris[1], Jimmy K. Hu [2,3,*], Neil H Shubin[1,*]

[1] Department of Organismal Biology and Anatomy, The University of Chicago, Chicago, IL, USA
[2]School of Dentistry, University of California Los Angeles, Los Angeles, California, USA
[3]Molecular Biology Institute, University of California Los Angeles, Los Angeles, California, USA

[*]Corresponding author(s)

Abstract

For decades, biologists have relied on confocal microscopy to understand cellular morphology and the fine details of tissue structure. However, traditional confocal microscopy of tissues have limited penetration depths of light ~ 100 µm due to tissue opaqueness. Researchers have, thus, developed tissue clearing protocols to be used with confocal microscopy, however, current clearing protocols are not compatible with labels of cell boundaries, especially at high enough resolution to precisely segment individual cells. In this work, we devise a method to retain markers of cell boundaries, and refractive index-match the tissues with water to enable tissue imaging at high magnification using long working distance water dipping objectives. The sub-micron resolution of these images allows us to automatically segment each individual cell using a trained neural network segmentation model. These segmented images can then be utilized to quantify cell properties and morphology of the entire three-dimensional tissue. As an example application, we first test our methodology on mandibles of mutant mice that express fluorescent proteins in their membranes. We then examine a non-model animal, the catshark, and explore the cellular properties of their dental lamina and dermal denticles, which are invaginating and evaginating ectodermal structures, respectively. We, thus, demonstrate that the technique presented here provides a powerful tool to quantify, in high-throughput, the 3D structures of cells and tissues during organ morphogenesis.

Introduction

Biologists have long visualized the microstructure of cells and tissues by acquiring thin sections that provide two-dimensional (2-D) maps of biological information. These maps can be further analyzed to understand spatial relationships of RNA transcripts, proteins, and cellular morphology and organization. However, to better image native tissue structures, images that contain three-dimensional (3-D) information are required. To acquire information of the inherently 3-D structure of tissues, scientists have used traditional approaches such as MRI, computed tomography and ultrasound imaging, but unlike optical microscopy, these traditional approaches are unable to provide submicron resolutions and single molecule imaging (*1*). Early methods to acquire 3-D optical microscopy images included serial 2-D sections, but the z-resolution of these reconstructed 3-D images was poor and limited to the slice thickness of the microtome. Now, with advances in fluorescence microscopy and computing power to handle large datasets, scientists are able to perform volumetric optical microscopic imaging to investigate 3-D cell and tissue microstructure (*2*). Native tissues, however, pose a complicated problem for optical microscopes: their composition of various lipids, proteins, minerals, pigments, among others components render the tissues optically opaque due to scattering and distortion of light from refractive index mismatch, which limits the penetration depth of light, and thus the optical imaging depth of tissues (*3*).

Efforts to reduce tissue opaqueness have been ongoing for at least a century, where early efforts primarily focused on matching the refractive index (RI) of the tissue to the RI of the medium surrounding the tissue; early improvements to this technique included bleaching, decalcifying, dehydrating, and removal of hydrophilic components from the tissues (*4*). In the past decade, optical clearing methods have accelerated. Researchers have used a combination of advanced chemical techniques to remove high RI particles, such as lipids and fibrous proteins, endogenous pigments with strong absorption, such as heme and melanin, and the use of more efficient and appropriate RI-matching chemical agents without damaging or altering the native

cell and tissue structures of interest (*3*). The combination of tissue clearing, fluorescence labeling (small-molecule dyes, tagged antibodies and fluorescent proteins), and efficient confocal and light-sheet microscopes has revolutionized the ability of scientists to visualize biological specimens (*5–8*).

One particularly intriguing application of deep-tissue volumetric imaging is the ability to fully appreciate 3-D cellular and tissue morphology, which bypasses the need to section through different angles/axes to piece together tissue morphology. By segmenting individual cells, scientists can now quantify individual 3-D cell properties such as volume, sphericity, and cell length/orientation instead of area, roundness, and other incomplete 2-D cell properties obtained from often oblique tissue slices. In addition, 3-D images also reveal morphological characteristics, such as protrusions and other cell-cell or cell-matrix interactions that would otherwise be lost. Recent advances in machine learning and neural network image processing techniques have improved our understanding of cell biology by accurately segmenting both individual nuclei and entire cell bodies in an automated fashion with little-to-no user input (*9*, *10*). Such tools now allow one to track the 3D morphology of thousands of cells at once.

We find that in order to image entire "cleared" tissue samples and to automatically segment each individual cell within the tissues, several requirements must be met: A) a high numerical aperture (N.A. ≥ 0.8), high magnification microscope objective of 25× or above is needed to obtain necessary axial resolution (Z-resolution) to properly segment cell boundaries; B) the objective must have a long working distance, or enough to image through the entire tissue, ideally >1 mm; C) the objective must be RI-matched to the RI of the tissue and the RI of the medium surrounding the tissue; D) the cells must be stained with an appropriate marker that delineates cell boundaries. Unfortunately, light-sheet microscopy does not offer the resolving power needed to segment individual cells, and there are currently extremely few confocal on the market that

fulfill criteria A-C: higher power oil and glycerol objectives are limited to short working distances, typically < 200 μm; and longer working distance, high refractive index objectives are limited to lower magnification, typically < 20×, and are not designed for confocal microscopes. Finally, segmenting cell boundaries by either cytoplasmic or cell membrane markers can be challenging. While transgenic model species expressing genetically encoded membrane-targeted fluorescent proteins is useful, cell boundaries in wild-type animals and non-model species must be externally labeled. To this end, lipophilic fluorescent dyes, such as DiI, and markers of filamentous actin (F-actin), such as phalloidin (*11*), are not compatible with existing clearing methods as lipids and/or staining signals are lost during the clearing process.

To overcome these limitations, we employ a novel combination of techniques. First, since we find phalloidin to be the most consistent marker for cell body segmentation for various animal species, we devise a method to retain its signal during the clearing process. Next, we aim to take advantage of high power, long working distance water immersion (dipping) objectives by digesting the tissues with proteinase K, which renders them optically transparent in water. To prevent the enzymatic digestion from completely dissolving structures of interest, the antibodies and other fluorescent small molecules are covalently bound into polyacrylamide network using a heterobifunctional linker (*12*). As a proof of principle, we use the developing mouse and catshark embryos as systems, focusing on oral dental lamina and dermal denticle structures. Our results showed that the described technique allows us to fully segment each individual cell in the tissues of interest and quantify their 3-D morphological characteristics with both speed and precision.

Results and Discussion

To fully understand how tissues develop, it is desirable to understand the shape of cells and structure of entire tissues in their native 3-D form. In mice, this is achievable using genetically

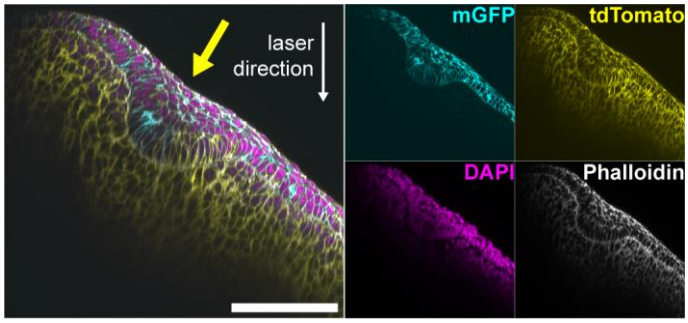

Figure 1. Virtual z-axis section of a 3D confocal volume without any tissue clearing. Image shows a sagittal view of a E12.5 *K14*^{Cre};*R26*$^{mT/mG}$ mouse mandibular incisor tooth bud (yellow arrow) counterstained with DAPI and phalloidin-Alexa Fluor 633. Epithelial cells are labelled by membrane GFP, mesenchymal cells retain expression of membrane tdTomato, while all cells are labelled by phalloidin. Scalebar: 100 µm.

encoded fluorescent proteins that label the cell membrane or nucleus. For example, *K14*^{Cre};*R26*$^{mT/mG}$ mice express a *Keratin 14* promoter-driven Cre recombinase that activates the expression of membrane GFP in ectodermally derived epithelial tissues, such as the developing dental epithelium. In mesenchymal cells where the Cre is inactive, membrane tdTomato is expressed. These signals can thus be used to delineate both individual epithelial and mesenchymal cells. We examined the development of the vertebrate tooth by obtaining individual 3-D cellular morphology, first using non-cleared tissues under conventional confocal microscopy. This allowed us to visualize the entire embryonic day (E) 12.5 incisor tooth bud, but the resolution of cells at a penetration depth beyond ~100 µm became severely limited (Figure 1).

To overcome the limitation of confocal penetration depth, we next incubated E12.5 *K14*^{Cre};*R26*$^{mT/mG}$ mouse mandibles in a refractive index matching solution, termed CUBIC-R (*13*), that rendered tissues optically transparent. To image these cleared tissues we utilized a 25×/0.8 glycerine immersion objective (Figure 2), and we were able to visualize cell boundaries and tissue structures at sub-micron resolutions and at z-depths beyond the incisor tooth bud, deep into the underlying mesenchyme (Figure 2A). Before RI-matching, we have also counterstained the tissues with DAPI and phalloidin, a small molecule toxin produced in death cap mushrooms, in order to

visualize the nucleus and filamentous actin (F-actin) respectively. However, while signals from genetically encoded fluorescence (membrane GFP and tdTomato) and DAPI staining were retained after RI-matching (Figure 2C), phalloidin staining was ultimately lost. This methodology is

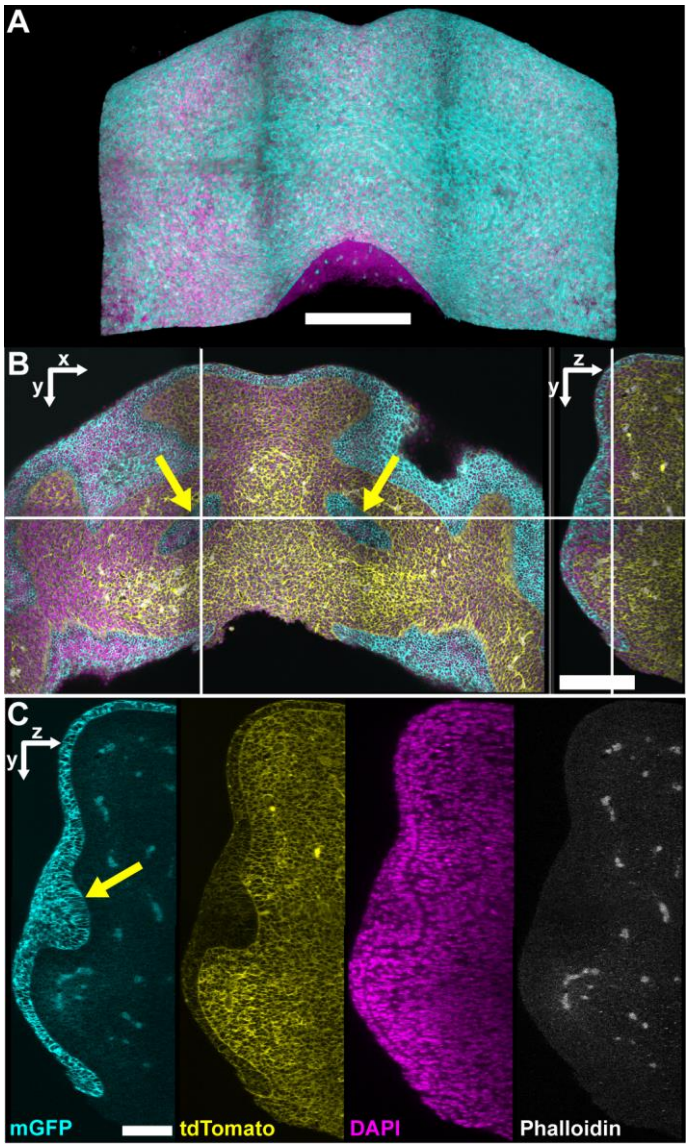

Figure 2. Example 3D confocal volume of E12.5 *K14*$^{Cre-}$;*R26*$^{mT/mG}$ mouse mandible counterstained with DAPI and phalloidin-Alexa Fluor 633, and cleared with CUBIC-R refractive index matching media. Image aquired using a 25× glycerine immersion objective. Yellow arrows indicate location of the incisor bud. A) Reconstructed 3D image of the dorsal view of the mandible. B) Virtual transverse (left) and sagittal (right) sections of the 3D confocal volume showing the incisor tooth bud. C) Single channel images of sagittal section. Epithelial cells are labelled by membrane GFP and mesenchymal cells retain expression of membrane tdTomato. Note that phalloidin stain is not maintained after tissue clearing. Scalebars: A) 300 µm; B) 200 µm; C) 100 µm.

therefore not applicable to certain dye-labelling in wild-type animals or non-traditional model animals.

To apply this methodology to animals that do not express fluorescent proteins in their membranes, we explored other methods to fluorescently tag cell boundaries. Motivated by the highly conserved nature of actin, and the non-species-specific binding of phalloidin (*14*), we sought to identify ways that would enable the retention of the phalloidin signal after optical clearing of the tissues. Inspired by previously reported techniques that stabilize phalloidin binding (*11*), we turned to the catshark embryos, a non-traditional model species, for proof-of-principle experiments and labelled the phalloidin-conjugated Alexa Fluor 488 fluorescent dye with an anti-Alexa Fluor 488 antibody (Figure 3A, B). After formaldehyde fixation, the antibodies and their respective conjugated fluorescent dyes were not affected by refractive index matching solutions (*13*) and the tissue can be cleared while maintaining patterns of phalloidin binding (Figure 3C). As such, embryonic

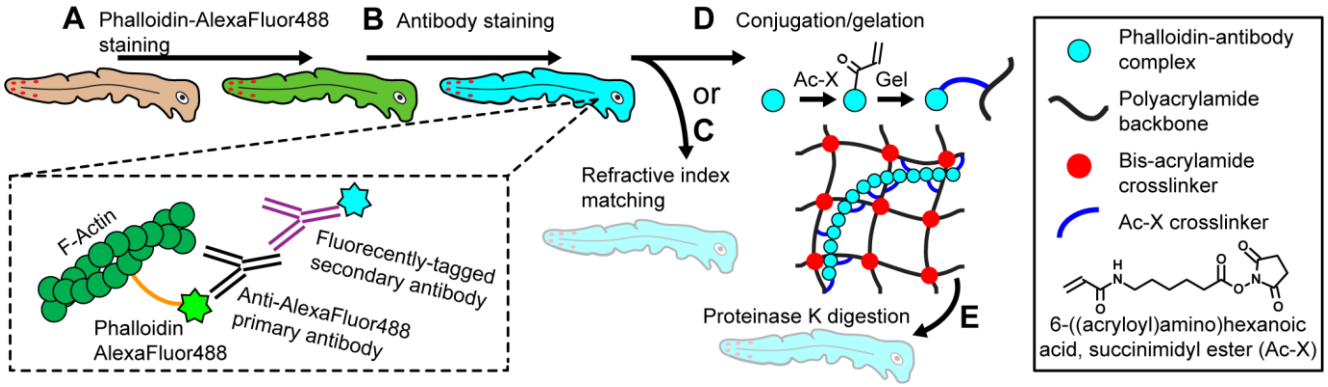

Figure 3. Schematic of phalloidin retention and tissue clearing process using catshark embryos as an example. A) After fixation, permeabilization, and blocking, tissues are stained with phalloidin conjugated to Alexa Fluor 488. B) Phalloidin is then antibody-tagged with anti-fluorescent dye (Alexa Fluor 488) primary antibodies, followed by fluorescently-tagged secondary antibodies. At this point, the sample can undergo refractive index-matching imaging. C) The tissue sample is then incubated in heterobifunctional linker (Ac-X) that converts primary amines on the antibodies to reactive acrylamide groups. These acrylamide groups are then polymerized along with acrylamide monomers and bis-acrylamide crosslinkers into a polyacrylamide hydrogel network. From here, the tissue can be digested with proteinase K to RI-match the tissue to water.

catsharks maintain the phalloidin signal after RI-matching and can be imaged at sub-micron resolutions at full tissue penetration depths using confocal microscopy (Figure 4A).

A major limitation of the protocol outlined in Figure 3A-C is that high powered (≥ 25×) glycerine or oil immersion objectives are typically manufactured with limited working distances (≤ 570 µm for Zeiss, Leica, and Nikon objectives) and that the full thickness of larger tissue samples cannot be imaged (Figure S1). Thus, we seek a method to utilize high magnification water immersion objectives with long, > 1 mm, working distances. To that end, we adapted protocols from the protein-retention Expansion Microscopy (proExM) technique (*6*, *12*, *15*), where, after antibody labeling, we conjugated the tissue proteins to a polyacrylamide hydrogel and subjected the tissue-gel construct to a nonspecific proteolytic digestion that renders the samples transparent and RI-matched to water (Figure 3D). Protein-gel conjugation is achieved using the heterobifunctional crosslinker 6-((acryloyl)amino)hexanoic acid, succinimidyl ester (AcX) that covalently substitutes primary amines of tissue protein and antibodies with reactive acrylamide groups. These reactive acrylamide groups then polymerize into the backbone of the polyacrylamide hydrogel. Once the tissues have been enzymatically digested, they can be imaged using water immersion objectives.

Using a 40× water immersion objective, we are able to successfully image, at high resolution and resolving power, tissues from catshark tail-tips that are hundreds of microns thick while maintaining the phalloidin signal (Figure 4B,C). The quality of the protein-retention, gel embedded images (Figure 3B) matches those of similarly sized samples cleared with RI-matching media CUBIC-R (Figure 3A). Since the gel embedded samples can be imaged with higher power objectives, the potential resolution of the images is higher, especially in the z-direction.

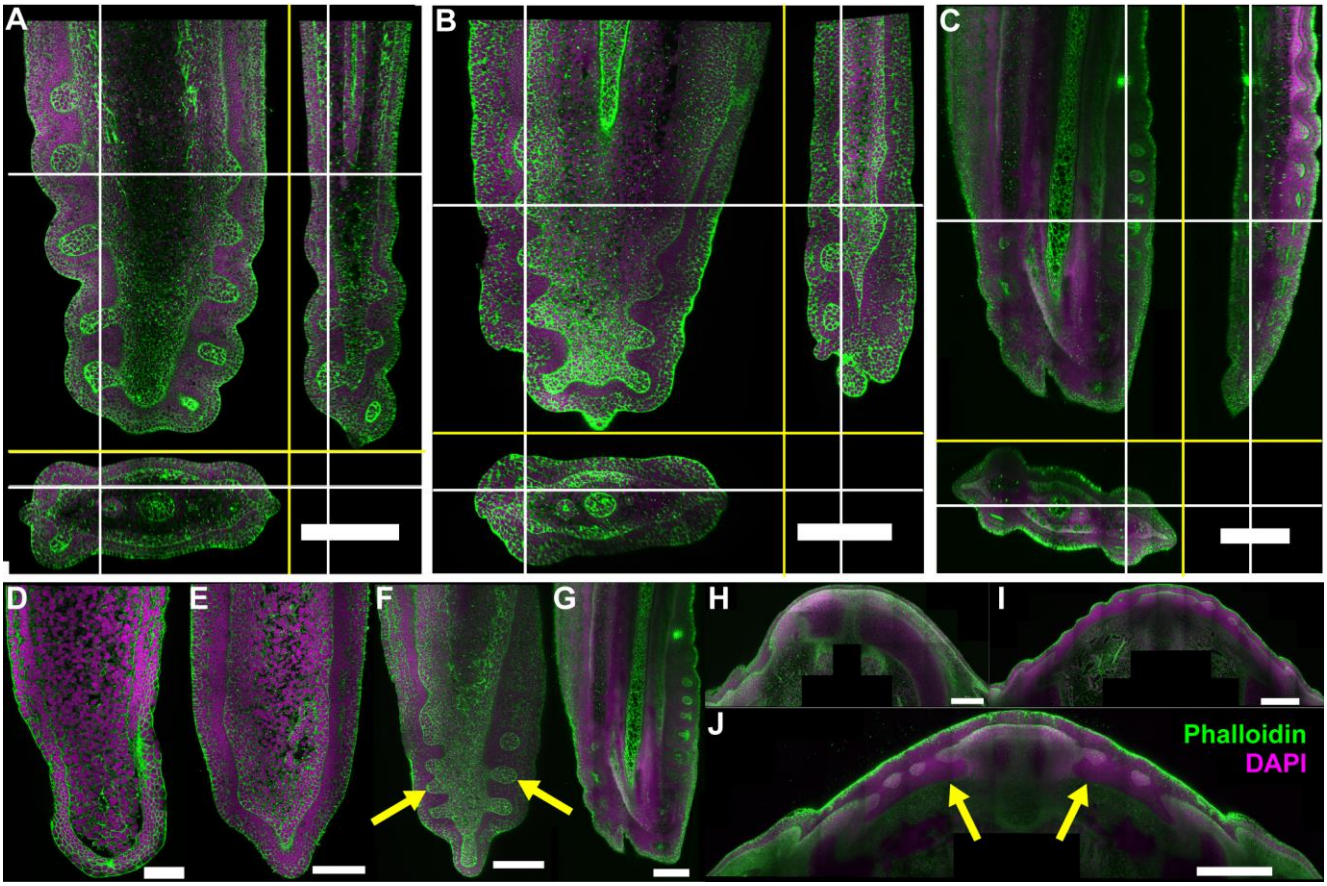

Figure 4. 3D confocal images of optically cleared catshark tissues with phalloidin retention, counterstained with DAPI. A-G) Tail tips showing the dermal denticles (yellow arrows) and; H-J) mandibles showing the dental lamina (yellow arrows). A-C) Orthogonal views of 3D confocal volumes. A) 27 mm catshark tail tip with phalloidin retention protocol and optically cleared with CUBIC-R refractive index matching media. Scalebar: 300 µm. B) 27 mm and C) 32 mm catshark tail tips with phalloidin retention protocol, polyacrylamide gel-embedded, and digested with proteinase K. D-J) Example virtual sagittal slices from 3D confocal volumes of D) 24 mm stage 27 shark tail, E) 25 mm stage 28 shark tail, F) 27 mm stage 29 shark tail, G) 32 mm stage 30 shark tail, and virtual frontal slices of H) 41 mm stage 31 shark mandible, I) 47 mm stage 32 shark mandible, and J) 50 mm stage 33 shark mandible. Scalebars: A,B) 300 µm; C) 600 µm; D) 80 µm; E) 150 µm; F) 250 µm; G) 300 µm; H) 300 µm; I) 400 µm; J) 500 µm.

To further assess the performance of the protein-retention, gel embedded technique in other tissues and embryonic stages, we imaged a series of catshark tail tip (Figure 4D-G), and mandibles (Figure 4H-J) at different ages, paying special attention to the comparison of the tail tip dermal denticles and mandibular dental lamina and tooth buds. We also tested the protein-retention gel embedded technique using E12.5 *K14*^{Cre};*R26*$^{mT/mG}$ mouse mandibles, where fluorescent proteins are genetically encoded (Figure S2). In all cases, we were able to obtain detailed 3-D images (Fig.).

We next assess our ability to segment individual cells after whole-tissue, high-resolution 3-D confocal images have been acquired. Using a stage 24 mm, stage 27 catshark tail tip as an example, we automatically segmented each individual cell within the tissue using a custom trained neural network segmentation model (*16*). The phalloidin channel (Figure 5A) served as the main input signal for cell boundaries and was sufficient for the custom trained model to successfully segment each individual cell within the tissue (Figure 5B). Cell

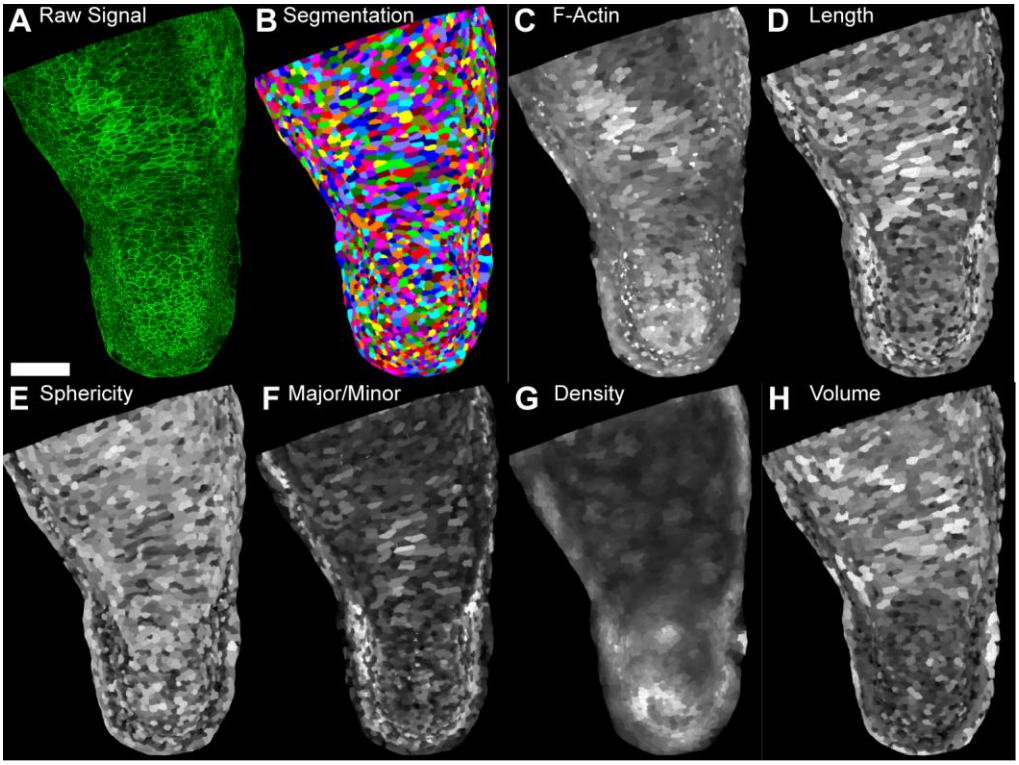

Figure 5. Example 24 mm stage 27 shark tail tissue processed with phalloidin retention protocol, polyacrylamide gel-embedded, and digested with proteinase K. Segmented cells using CellPose and measured properties of each 3D volumetric cell. Volumetric images of A) input phalloidin fluorescence signal, and B) individually segmented cells. C-H) Heat maps of cellular morphology and phalloidin intensity. C) Average phalloidin intensity per cell, D) length of longest principal axis of each cell, E) cell sphericity, F) ratio of the largest/smallest principal axes, G) local cell density in units of cells/volume, and H) cell volume. Scalebar 100 μm.

segmentations also allow further computational processing to obtain cell-by-cell data such as: average F-actin concentration per cell (Figure 5C); length of the longest principle axis of the cell (Figure 5D); the sphericity of the cell (Figure 5E); the ratio of the longest and shortest (major/minor) principle axes of the cell (Figure

5F); the local cell density, in units cells/unit volume (Figure 5G); and the volume of each cell (Figure 5H). In Figure 5, however, we showcase the properties of the cells on the surface of the tissue, not the interior.

To obtain cellular information within the tissue interior, we produced virtual sections through the segmented and cell property-labeled images to obtain 2-D snapshots of 3-D cellular morphology information about cells from a particular tissue region and view (Figure 6). Epithelial morphogenic processes, fundamentally rely on the bending of epithelial sheets that, in simple terms, can occur by two different modes: invagination into the underlying tissue; and evagination outwards from the epithelial surface (*17*), however, the mechanisms by which epithelial bending direction is not well understood. Using the catshark mandibular dental lamina

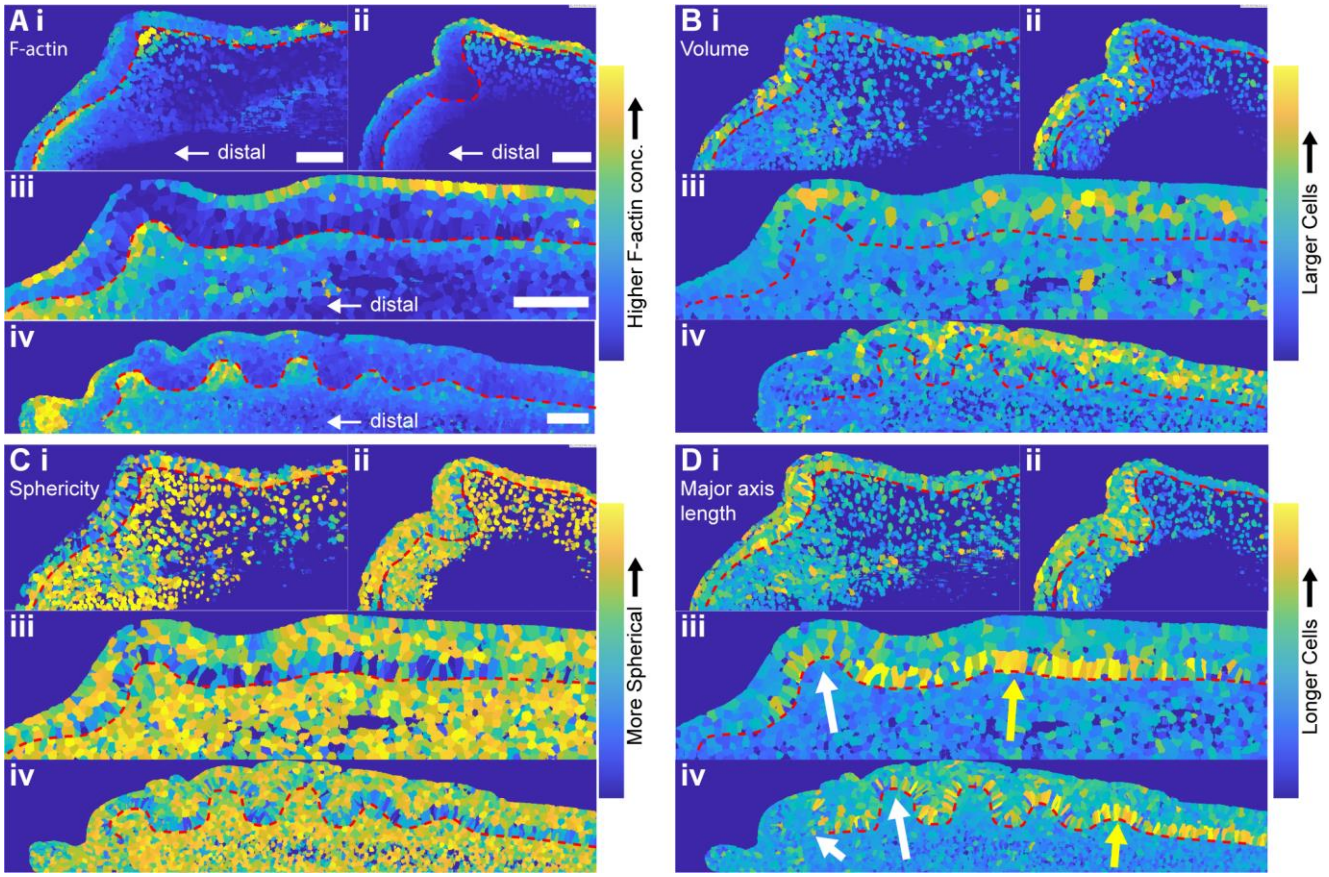

Figure 6. Example heat maps of 3D cell properties mapped on a cell by cell basis from 3D volumetric images. Sections from i) 43 mm shark mandible, ii) 47 mm shark mandible, iii) 25 mm shark tail, iv) 28 mm shark tail. Cell-by-cell measurements of A) average F-actin staining intensity, B) cell volume, C) cell sphericity, and D) length of the longest principal axis of the cells. Scalebars 100 μm.

(Figure 6i,ii) and tail-tip dermal denticles (Figure 6iii, iv) as examples, we compared the cellular properties of both invaginating (dental lamina) and evaginating (dermal denticles) tissue structures. To explore the cell behaviors that could lead to these two different types of epithelial bending, we examined the distribution of F-actin across the tissues (Figure 6A), cellular volume (Figure 6B), the cell sphericity (Figure 6C), and the length of the longest principle axis of the cells (Figure 6D). The first signs of tooth development and invagination come when the local epithelium thickens (*18*) and the basal epithelial cells elongate (*19*), however, it is less clear if basal epithelial cell elongation also precedes epithelial evagination. We first confirmed that the basal epithelial cells of the catshark mandibular dental lamina are elongated in early (Figure 6Di) and later stage (Figure 6Dii) dental lamina. Cell sphericity is a similar metric that measures how spherical or elliptical a cell is; thus, we expect that basal epithelial cells at the dental placode to be more elliptical. Indeed, we find that the same cells that are elongated (Figure 6Di, ii) are also more elliptical (Figure 6Ci, ii). Next, we find that similar to the dental placode, the basal epithelial cells of the evaginating tail-tip dermal denticles also locally elongate in regions of placode formation in both early (Figure 6Div) and later stage denticles (Figure 6Diii). Interestingly, the basal epithelial cells of newly formed dermal denticle placodes (Figure 6Diii, iv yellow arrows) are more elongated than older, more distal placodes that have more fully evaginated (Figure 6Diii, iv white arrows), where elongated cells are also typically more elliptical (Figure 6C). Next, we are interested to see if cell growth, by observing local changes in cell volume predicted epithelial bending. Surprisingly, we find no definitive patterns of cell volume in neither the catshark dental lamina nor dermal denticles (Figure 6B). Finally, we look at the distribution of F-actin staining intensity on a cell-by-cell basis by averaging the staining intensity through the whole volume of each cell (Figure 6A). Mesenchymal cells underlying the dermal denticles exhibit elevated F-actin staining intensity that indicates elevated cell tension (Figure 6Aiii, iv yellow arrows). In contrast, we see no particular pattern of F-actin staining intensity in the dental lamina placodes (Figure 6Ai, ii).

Conclusions

In this work we have developed a method to image cell boundaries at sub-micron resolutions. While genetic model organisms can be bred to express fluorescent proteins in their cell membranes, wild type and non-traditional model animals do not have this luxury. Given that phalloidin, which selectively labels F-actin in most species, acts as a good marker of cell boundaries, we adapted a method to retain phalloidin staining during tissue clearing. These phalloidin-retained tissues were further processed and optically cleared by two different methods: the embryonic tissues could simply be incubated in a refractive index-matching solution; or embedded into a polyacrylamide gel, covalently binding the tissue proteins to the gel backbone, and digesting the remaining tissue so that tissue was refractive index-matched with water. The latter method allowed us to utilize high magnification, long working distance water dipping objectives to image the entire tissue. The subsequent images were then automatically segmented using a user-trained neural network segmentation model, which output each individual cell volume of the tissues. As an example application, we examined epithelial bending of the invaginating catshark dental lamina and their evaginating dermal denticles. This data leaves us to believe that basal epithelial cells elongate in regions of high in-plane epithelial compression, and that increased F-actin activity in the mesenchymal portion of the dermal denticle placode constricts the mesenchyme, causing it to buckle outwards. We expect that the techniques devised in this work, will help developmental biologists apply more quantitative measures of 3D cell morphology to understand tissue morphogenesis.

Funding

SCPN was supported by the National Institute of Dental & Craniofacial Research of the National Institutes of Health under Award Number F32DE030004. JKH was supported by NIDCR R01DE027620. NHS acknowledges support from the Biological Sciences Division of the University of Chicago and the Brinson Foundation.

Materials & Methods

Materials

Tricaine (Syndel), Phosphate Buffered Saline (PBS) (Fisher Scientific), paraformaldehyde (PFA, Thermo Scientific), goat serum (Gibco), bovine serum albumin (BSA, Fisher Scientific), Triton X-100 (Fisher Scientific), phalloidin conjugated to either Alexa Fluor™ 488 (Thermo Fisher A12379), or Alexa Fluor™ 633 (Thermo Fisher A22284), 4′ ,6-diamidino-2-phenylindole (DAPI, Biotium 40009), rabbit anti-Alexa Fluor™ 488 (Thermo Fisher A11094), goat anti-rabbit 633, (Biotium 20122), 35 mm glass bottom dish (Thermo Scientific), low melting point agarose (Thermo Scientific), #1.5 coverglass (Fisher Scientific), dimethyl sulfoxide (DMSO, Thermo Scientific), acrylamide (AAm, Thermo Scientific), bis-acrylamide (BAAm, Thermo Scientific), ammonium persulfate (APS, Acros Organics), tetramethylethylenediamine (TEMED, Thermo Scientific), 4-hydroxy-2,2,6,6-tetramethylpiperidin-1-oxyl (TEMPO, Thermo Scientific), and Proteinase K (Invitrogen) were used as purchased.

A wash solution of 0.1% Triton X in 1× PBS (PBST), refractive-index matching solution (45 w/v% antipyrine (Thermo Scientific), 30 w/v% nicotinamide (Thermo Scientific), and 0.5 v/v% N-butyldiethanolamine (Thermo Scientific) in distilled water: termed CUBIC-R (*13*)), were made fresh in the lab. Digestion buffer consisting of Triton X, ethylenediaminetetraacetic acid (EDTA, Sigma), tris(hydroxymethyl)aminomethane (Tris hydrochloride, Roche), and sodium chloride (Sigma) was prepared as previously described (*12*).

6-((Acryloyl)amino)hexanoic Acid, Succinimidyl Ester (AcX, CAS number: 63392-86-9) was synthesized as previously described (*20*, *21*).

Collection of embryos and fixation

Mice: $K14^{Cre}$;$R26^{mT/mG}$ mice were generated by crossing $K14^{Cre}$ (MGI:2445832) (*22*) with $R26^{mT/mG}$ (MGI:3716464) (*23*). C57BL/6 were purchased from JAX. All mice were group housed and genotyped as previously published. To generate embryos for experiments, mice were mated overnight, and noon of the day of vaginal plug discovery was designated as E0.5. Pregnant females were euthanized by CO_2 followed by cervical dislocation. Both male and female GFP-positive $K14^{Cre}$;$R26^{mT/mG}$ embryos or C57BL/6 embryos were selected at random and used for experiments. Mandibles were dissected out in PBS and fixed in freshly made 4% paraformaldehyde (PFA) in 1× PBS for 12 hours on a rocker at 4°C. The samples were then washed in 1× PBS three times for 10 minutes each and stored in 0.5% PFA at 4°C until use. All mice were maintained in the University of California Los Angeles (UCLA) pathogen-free animal facility. All animal procedures were conducted in compliance with animal protocols approved by the UCLA Institutional Animal Care and Use Committee (Protocol Number ARC-2019-013).

Sharks: Fertilized eggs of small spotted catshark (*Scyliorhinus rotifer)* were obtained from the Marine Biological Laboratory, Woods Hole, MA (stages 28-32). Embryos were mechanically extracted and placed in a 0.5% Tricaine solution diluted in in 1× PBS solution for thirty minutes. Embryos were then fixed in freshly made 4% PFA in 1× PBS for 24 hours on a rocker at 4° C.

Fixed samples were washed in 1× PBS four times for 1h each. Mandibles and tails were dissected out and stored in 1× PBS. From this point forward, samples were protected from light during.

Immunofluorescence labeling and tissue clearing.

Antibody and fluorescence labeling. Mouse mandibles and shark mandibles and tails were first incubated in blocking buffer (5% goat serum, 1% BSA, 0.3% Triton X in 1× PBS) for 24 hours on a rocker at 4° C. Next, the samples were incubated in phalloidin conjugated to either Alexa Fluor™ 488 or 633 (1:200) and DAPI (0.1 mg/mL) in blocking buffer for 7 days on a rocker at 4° C. The samples were then washed in PBST three times for 1h each before storage in 1× PBS. Samples receiving no further antibody treatment were either cleared or imaged directly. Samples were then stained with anti-fluorophore antibody (1:200) in blocking buffer for 3 days on a rocker at 37° C protected from light. The samples were then washed in PBST three times for 1h each. The labeled samples were then stained with secondary antibody (1:300) in blocking buffer for 3 days on a rocker at 37° C. The samples were then washed in PBST three times for 1h each.

Tissue clearing. Tissues were rendered optically transparent by two different methods: the first renders the samples optically transparent by simply immersing them in an aqueous-based high refractive index solution; the second covalently binds the antibodies into a 3D polymer network and enzymatically digests the remaining tissue.

(A) To render tissues optically transparent in a high-refractive index solution, fluorescently labeled samples were first fixed in freshly made 1% PFA in 1× PBS for 24 hours on a rocker at 4° C. Samples were then washed for 2h in 1× PBS before immersing in a for 1-3 days (depending on the size of the embryonic sample) in CUBIC-R to render the tissues optically transparent for three-dimensional imaging. Samples were mounted on a 35 mm coverglass bottom dish suspended in a 0.5% agarose solution in CUBIC-R to avoid movement of the sample during the imaging process. The mounted samples were then covered with a coverglass before imaging.

(B) To render tissues optically transparent in a low refractive index aqueous solution, fluorescently labeled samples were incubated in a freshly made solution of the heterobifunctional linker AcX. A stock solution of 50 mg/mL AcX in anhydrous DMSO was freshly prepared before diluting 10-fold in PBS. Samples were immediately immersed in the AcX solution for 24 hours on a rocker at 22° C. The functionalized tissues were then washed with PBST for 2h and immersed in a cold polyacrylamide pre-polymer solution consisting of AAm (9.6 w/v%), BAAm (0.25 w/v%), TEMPO (0.75 w/v%), APS (0.2 w/v%), and TEMED (0.2 v/v%) in 1× PBS for 4h in an ice bath, while rocking. The pre-polymer solution was replaced and the samples were placed between two glass slides with 1 mm spacers, which was filled with the pre-polymer solution. The glass slide-sample sandwiches were then incubated at 37° C for 1h to polymerize the polyacrylamide gels. The tissue-gel construct was then trimmed and immersed in a solution of Proteinase K in digestion buffer (0.2 mg/mL) and incubated for 48h on a rocker at 22° C, or until the tissue was rendered

optically transparent. The tissues were then washed with 1× PBS three times for 1h each. Samples were mounted in a 35 mm plastic dish suspended in a 0.5% agarose solution in 1× PBS before imaging.

Confocal imaging

Samples were imaged with a Zeiss confocal laser scanning microscopes (LSM 900) equipped with either a Plan-Apochromat 25x/0.8 glycerine immersion objective with a working distance (WD) of 0.57 mm or a Plan-Apochromat 40x/1.0 water dipping objective, WD 2.5mm. A pinhole of 1 AU was used. Three dimensional, whole-tissue volumes were acquired using a combination of Z-stacks and image tiling.

Image Processing and segmentation.

Images were processed and visualized with Zen (Zeiss), ImageJ and Imaris. The multi-tiled images were stitched with the ImageJ plugin BigStitcher (*24*). Certain contrast adjustments were applied to enhace details for visualization and segmentation, but not for signal quantification. The stitched images were reoriented and cropped to contain the region of interest and reduce file size and segmented using CellPose (*9*). Before segmentation the neural network model was trained using a subset of images where the F-actin signal was used as the primary channel, and the DAPI signal was used as the secondary (*16*). Training was repeated and refined as needed to produce properly segmented 3D cell volumes. Segmented volumes were output as multi-Z masks tiff file.

Once the individual cells were segmented, the mask files were imported into MATLAB the properties of 3-D volumetric image regions were measured with the regionprops3 algorithm. A piece of custom MATLAB code was then utilized to reconstruct 3-D heatmaps of the segmented cells labeled with different morphological features (volume, sphericity, F-actin concentration, cell length, etc…).

References

1. D. S. Richardson, W. Guan, K. Matsumoto, C. Pan, K. Chung, A. Ertürk, H. R. Ueda, J. W. Lichtman, Tissue clearing. *Nat. Rev. Methods Prim.* **1**, 84 (2021).
2. D. S. Richardson, J. W. Lichtman, Clarifying Tissue Clearing. *Cell*. **162**, 246–257 (2015).
3. T. Yu, J. Zhu, D. Li, D. Zhu, Physical and chemical mechanisms of tissue optical clearing. *iScience*. **24**, 102178 (2021).
4. A. Azaripour, T. Lagerweij, C. Scharfbillig, A. E. Jadczak, B. Willershausen, C. J. F. Van Noorden, A survey of clearing techniques for 3D imaging of tissues with special reference to connective tissue. *Prog. Histochem. Cytochem.* **51**, 9–23 (2016).
5. K. Chung, J. Wallace, S.-Y. Kim, S. Kalyanasundaram, A. S. Andalman, T. J. Davidson, J. J. Mirzabekov, K. A. Zalocusky, J. Mattis, A. K. Denisin, S. Pak, H. Bernstein, C. Ramakrishnan, L. Grosenick, V. Gradinaru, K. Deisseroth, Structural and molecular interrogation of intact biological systems. *Nature*. **497**, 332–337 (2013).
6. F. Chen, P. W. Tillberg, E. S. Boyden, Expansion microscopy. *Science (80-.).* **347**, 543–548 (2015).
7. E. A. Susaki, K. Tainaka, D. Perrin, F. Kishino, T. Tawara, T. M. Watanabe, C. Yokoyama, H. Onoe, M. Eguchi, S. Yamaguchi, T. Abe, H. Kiyonari, Y. Shimizu, A. Miyawaki, H. Yokota, H. R. Ueda, Whole-Brain Imaging with Single-Cell Resolution Using Chemical Cocktails and Computational Analysis. *Cell*. **157**, 726–739 (2014).
8. N. Renier, Z. Wu, D. J. Simon, J. Yang, P. Ariel, M. Tessier-Lavigne, iDISCO: A Simple, Rapid Method to Immunolabel Large Tissue Samples for Volume Imaging. *Cell*. **159**, 896–910 (2014).
9. C. Stringer, T. Wang, M. Michaelos, M. Pachitariu, Cellpose: a generalist algorithm for cellular segmentation. *Nat. Methods*. **18**, 100–106 (2021).
10. S. Berg, D. Kutra, T. Kroeger, C. N. Straehle, B. X. Kausler, C. Haubold, M. Schiegg, J. Ales, T. Beier, M. Rudy, K. Eren, J. I. Cervantes, B. Xu, F. Beuttenmueller, A. Wolny, C. Zhang, U. Koethe, F. A. Hamprecht, A. Kreshuk, ilastik: interactive machine learning for (bio)image analysis. *Nat. Methods*. **16**, 1226–1232 (2019).
11. C. E. Park, Y. Cho, I. Cho, H. Jung, B. Kim, J. H. Shin, S. Choi, S.-K. Kwon, Y. K. Hahn, J.-B. Chang, Super-Resolution Three-Dimensional Imaging of Actin Filaments in Cultured Cells and the Brain via Expansion Microscopy. *ACS Nano*. **14**, 14999–15010 (2020).
12. S. M. Asano, R. Gao, A. T. Wassie, P. W. Tillberg, F. Chen, E. S. Boyden, Expansion Microscopy: Protocols for Imaging Proteins and RNA in Cells and Tissues. *Curr. Protoc. Cell Biol.* **80** (2018), doi:10.1002/cpcb.56.
13. E. A. Susaki, C. Shimizu, A. Kuno, K. Tainaka, X. Li, K. Nishi, K. Morishima, H. Ono, K. L. Ode, Y. Saeki, K. Miyamichi, K. Isa, C. Yokoyama, H. Kitaura, M. Ikemura, T. Ushiku, Y. Shimizu, T. Saito, T. C. Saido, M. Fukayama, H. Onoe, K. Touhara, T. Isa, A. Kakita, M. Shibayama, H. R. Ueda, Versatile whole-organ/body staining and imaging based on electrolyte-gel properties of biological tissues. *Nat. Commun.* **11**, 1982 (2020).
14. T. D. Pollard, J. A. Cooper, Actin, a central player in cell shape and movement. *Science (80-.).* **326**, 1208–1212 (2009).
15. P. W. Tillberg, F. Chen, K. D. Piatkevich, Y. Zhao, C. C. Yu, B. P. English, L. Gao, A. Martorell, H. J. Suk, F. Yoshida, E. M. Degennaro, D. H. Roossien, G. Gong, U. Seneviratne, S. R. Tannenbaum, R. Desimone, D. Cai, E. S. Boyden, Protein-retention expansion microscopy of cells and tissues labeled using standard fluorescent proteins and

antibodies. *Nat. Biotechnol.* **34**, 987–992 (2016).

16. M. Pachitariu, C. Stringer, Cellpose 2.0: how to train your own model. *Nat. Methods*. **19**, 1634–1641 (2022).
17. Y. Wang, D. Stonehouse-Smith, M. T. Cobourne, J. B. A. Green, M. Seppala, Cellular mechanisms of reverse epithelial curvature in tissue morphogenesis. *Front. Cell Dev. Biol.* **10**, 1–13 (2022).
18. J. Pispa, I. Thesleff, Mechanisms of ectodermal organogenesis. *Dev. Biol.* **262**, 195–205 (2003).
19. J. Li, L. Chatzeli, E. Panousopoulou, A. S. Tucker, J. B. A. Green, Epithelial stratification and placode invagination are separable functions in early morphogenesis of the molar tooth. *Development*. **143**, 670–681 (2016).
20. S. C. P. Norris, J. Soto, A. M. Kasko, S. Li, Photodegradable Polyacrylamide Gels for Dynamic Control of Cell Functions. *ACS Appl. Mater. Interfaces*. **13**, 5929–5944 (2021).
21. D. D. Pless, Y. C. Lee, S. Roseman, R. L. Schnaar, Specific cell adhesion to immobilized glycoproteins demonstrated using new reagents for protein and glycoprotein immobilization. *J. Biol. Chem.* **258**, 2340–9 (1983).
22. H. R. Dassule, P. Lewis, M. Bei, R. Maas, A. P. McMahon, Sonic hedgehog regulates growth and morphogenesis of the tooth. *Development*. **127**, 4775–4785 (2000).
23. M. D. Muzumdar, B. Tasic, K. Miyamichi, L. Li, L. Luo, A global double-fluorescent Cre reporter mouse. *genesis*. **45**, 593–605 (2007).
24. D. Hörl, F. Rojas Rusak, F. Preusser, P. Tillberg, N. Randel, R. K. Chhetri, A. Cardona, P. J. Keller, H. Harz, H. Leonhardt, M. Treier, S. Preibisch, BigStitcher: reconstructing high-resolution image datasets of cleared and expanded samples. *Nat. Methods*. **16**, 870–874 (2019).